Journal of the European Ceramic Society 21 (2001) 1205–1212

www.elsevier.com/locate/jeurceramsoc

Numerical simulation of the thermal shock of alumina disks with different surface finish

A.G. Tomba M. *, A.L. Cavalieri

Instituto de Investigaciones en Ciencia y Tecnología de Materiales, INTEMA, Av. J.B. Justo 4302 (7600) Mar del Plata, Argentina

Received 30 September 2000; accepted 21 November 2000

Abstract

Disks of commercial alumina were fabricated by slip casting and sintering. Two surface treatments were performed: a coarse machining, using a diamond wheel (70 grit) and a fine one with SiC papers (120/320 grit). Residual stresses were measured by X-ray diffraction and the fracture strength of the specimens were determined in biaxial flexion using a ball on discontinuous ring fixture. The thermal shock resistance of the disks was evaluated by sudden cooling with a high-velocity air jet. The temperature differential between the disk and the air jet was incremented in 10°C until crack propagation was detected and the critical temperature differential (ΔT_C) was determined. Temperature and stress distributions during air impinging were calculated using a finite element analysis. Three models were proposed for the calculations and the results were analysed comparatively. Experimental data (ΔT_C values and crack patterns) were explained on the basis of the calculated stresses.

Keywords: Al_2O_3; Stress calculations; Surfaces; Thermal shock resistance

1. Introduction

The main advantages of ceramics used in severe conditions of service (high temperature and corrosive environments) are their chemical inertia, refractoriness and excellent mechanical properties at high temperatures. However, these materials can suffer damage or complete fracture when they are subjected to sudden temperature gradients (thermal shock).

The practical significance to study the thermal shock behaviour of ceramics has been associated with the great complexity of the material degradation under these conditions. Thus, therefore, there is not a unique and simple thermal shock test that yields quantitative and easily extrapolable results. The data are closely linked to the experimental conditions and their analysis can not be done by abstracting the experimental aspects. Recent studies have been based on the calculation of the stresses arising during the thermal shock by the application of more realistic models that simulate the actual thermomechanical conditions with the minor simplifications. The knowledge of the actual thermal stress that is undergone by the specimen has made it possible to achieve an insight into this complex behaviour. Novel techniques have been designed to satisfy the requirements of these approaches, specially in regard to controlled boundary conditions[1–11].

The objective of the present work is to simulate the cooling of ceramic disks with different surface finish using a finite element thermomechanical analysis. These numerical results are used to account for thermal shock resistance and fracture features. Three alternative models are proposed for the calculations and they are evaluated keeping in mind their explanatory potential.

2. Experimental procedure

2.1. Preparation of specimens

Disks (diameter: 35.00±0.02 mm, height: 2.60±0.01 mm) were fabricated by slip casting of an aqueous suspension of a commercial high purity alumina powder (Reynolds RC-HP DBM, $D_{50}=0.35$ μm, $S_e=7.3$ m^2/g).[12] The green samples were treated at 900°C, 1 h and ground with SiC papers (120, 320 and 600 grit) before

* Corresponding author. Tel.: +54-223-4816600; fax: +54-223-4810046.

E-mail address: agtomba@fi.mdp.edu.ar (A.G. Tomba M.).

0955-2219/01/$ - see front matter
PII: S0955-2219(00)00340-X

sintering at 1600°C, 2 h (heating rate of 2°C/min). The density of the sintered material was 99.5% and its resulting microstructure was homogeneous, with equibiaxial and elongated grains (mean size of 3.46±2.27 μm) and few intergranular pores.

Two different surface treatments were performed: coarse abrasive machining (C) and fine abrasive machining (F). The C operation was carried out using a planetary grinding machine equipped with a resin-bonded diamond wheel of 70 grit with a feed rate of 300 mm/min, an infeed of 0.05 mm and a wheel speed of 3800 rpm. The F finish was achieved using a semi-automatic polishing machine, a plate speed of 125 rpm and SiC paper of 120 and 320 grit, consecutively. Kerosene and water were employed as coolant/lubricant in C and F procedures, respectively.

2.2. Residual stresses and fracture strengths

The residual stresses produced by machining and the mechanical strength of C and F disks were determined previously.[13]

Residual stresses were determined by the $\sin^2\psi$ technique of X-ray diffraction with CrK_α radiation (90% penetration ≈8 μm). The values were in compression for both C and F specimens being higher for the first ones. The values obtained for {1 0 10} and {1 1 9} diffraction planes were −147.94±11.56 and −89.75±4.73 MPa for the C surface and −91.28±10.24 and −60.9±7.21 MPa for the F one, respectively.

The mechanical strength of specimens was measured in biaxial flexure employing a ball on a discontinuous ring fixture (ball diameter: 8.04±0,02 mm, ring diameter: 19.50±0.1 mm). The fracture strength (σ_F) obtained was 296±59 MPa for C specimens and 220±66 MPa for F ones.

2.3. Thermal shock test

The disks mounted horizontally on a refractory material, with the machined surface disk as the upper one, were tested.[1,3,14] The specimen was heated in an electrical furnace up to a predetermined temperature (T_i), allowed to equilibrate (90 min) and subjected to a sudden temperature change using a high-velocity air jet (330 m/min) at room temperature (T_0 = 26–27°C). The air was channelled onto the disk centre during 20 s, using a silica tube (inner radius, r_0 = 1.79±0.02 mm) placed at 90° and 3 mm (H) above the tested surface ($H/2r_0$ = 0.84). The Reynolds number calculated at the tube exit (Re_0) was 7×10^4 defining a turbulent regime for the air flow.[15,16]

After quenching, the specimen was cooled up to room temperature and examined for crack extension. If no cracking occurs, the temperature differential between the disk and the air jet was incremented in 10°C until crack propagation was detected. The thermal shock resistance ΔT_C, defined as the difference T_C-T_0 where T_C is the value of T_i when cracks are produced (crack initiation condition), was evaluated using this method.

During the air impinging, the temporal variation of the temperature was recorded on the lower specimen surface at the central point and at a peripheral one (located 14.5 mm from the centre). Fast response Pt-10%Rh/Pt thermocouples calibrated against known melting point standards and being accurate to ±2°C, were used. The heat transfer coefficient was estimated employing these registers together with the calculated ones. The crack propagation was detected as a sudden drop in the temperature register from which the fracture time was determined.

2.4. Numerical calculation of temperature and stress distributions

The temporal and spatial temperature and stress distributions in the specimen subjected to thermal shock were calculated by a finite element method, using a commercial code (LUSAS) and a thermomechanical semi-coupled analysis. Three models A, B and C that differ in thermal boundary conditions were used. Thermal distributions were analysed in previous works.[17,18]

Because of the axial symmetry of the test, only a half of the middle section of the disk (models A and B) and both the disk and the refractory material (model C) were simulated as a bidimensional axisymetric problem. The meshes were regular, with parabolic square elements (432 elements for models A and B and 576 elements for model C) and a higher discretization in the jet radius region (element length in jet region 4.4 times smaller than element length beyond).

The thermomechanical properties of alumina were taken from the literature[19] and the temperature dependency was considered except for Poisson modulus. Properties of the refractory material at 200°C were used for the calculation and the data were also taken from literature.[20,21]

2.4.1. Estimation of the heat transfer coefficient

The coefficient governing the convective heat transfer on the specimen surface, h, was estimated in previous works[17,18] by fitting the calculated temperature profiles with those measured during the test. The radial variation of the heat transfer coefficient was simulated by two alternative functions labelled as 1 and 2. The simplified function 1 considers a uniform coefficient in the jet radius region and a flow attenuation beyond it, according to Eq. (1):

$$h(r) = h_0^{(1)} \qquad 0 \leqslant r \leqslant r_0$$
$$h(r) = \frac{h_0^{(1)}}{r} r_0 \quad r_0 < r \leqslant R \tag{1}$$

where r_0 is the jet radius, R is the disk radius and $h_0^{(1)}$ is the value of h in the impinging jet region, which was considered as the fitting parameter. Function 2 considers the increment of h beyond the stagnation region[15,16,22] and its diminution toward the disk periphery, according to the Eq. (2):

$$h(r) = h_0^{(2)} \qquad 0 \leqslant r \leqslant r_0$$
$$h(r) = \frac{h_0^{(2)}}{r} r_0 \qquad r_0 < r \leqslant r_C \tag{2}$$
$$h(r) = \frac{h_0^{(2)'}}{r} r_0 \qquad r_C < r \leqslant R$$

where r_C is the value of the radius where the coefficient changes. The fitting parameters were $h_0^{(2)}$, $h_0^{(2)'}$ and r_C.

2.4.2. Numerical simulation models (boundary conditions)

Three models, A, B and C were proposed that differ in thermal boundary conditions of the upper and lower specimen surfaces, being equivalent with respect to the other features. The boundary conditions are closer to the actual ones in the order: A < B < C.

The three simulation models considered a flow impinging onto the upper surface of the disk, with a convective heat transfer coefficient invariant with the temperature during the quenching. Model A considers the function 1 for the attenuation of h along the radius of the disk and adiabaticity at the lower surface, dispirsing the heat conduction between the specimen and the refractory material. Model B differs from A in that it considers the turbulence increment beyond the stagnation region and its effects on the h values through function 2. Model C is analogous to B, in regard to the variation of h according to function 2, but it additionally considers the heat transfer by conduction from the refractory material. The lower surface of the disk was adiabatic for models A and B. Conversely, in model C, the heat conduction by contact with the refractory material was permitted ('gap conductance'$\approx 10^3$ W/m^2°C[18]). The remainder boundaries were considered adiabatic.

For the stresses evolution, an axisymetric deformation problem was considered. Both, alumina and refractory materials were taken as elastic, linear and isotropic. In the three models, the radial displacement for the nodes located on the central axis in the disk as much as in the refractory material were constrained.

3. Results and discussion

3.1. Experimental data

The values of ΔT_C obtained from thermal shock tests of alumina specimens with C and F surface treatments were present and analysed previously,[23] being 765 ± 51 and 916 ± 54°C, respectively. The results make evident the dependence of the thermal shock behaviour on the surface finish, being the thermal shock resistance higher for F disks. Based on the mechanical strength together with the parity hypothesis,[1] this result is unexpected and some reasons to this behaviour are analysed elsewhere.[23] Fracture times were in the range 3–15 s.

The crack patterns for the broken disks and their fractographic analysis have been previously reported.[14] The fracture exhibited similar features for both machining specimens: circular and radial cracks, high fragmentation (3–7 parts), marked crack deflections (tortuosity) and irregular fracture surfaces. When incomplete fracture occurred, cracks did not reach the disk periphery, nevertheless they always went through the thickness of the specimen.

3.2. Numerical analyses

Taking in mind the temperature dependence of h, three representative values of T_i were selected for fitting: 770, 850 and 940°C for C and 870, 920 and 980°C for F. The experimental curves of the temperature evolution for each T_i were the average of all the tests carried out at this temperature for the same kind of specimens.

3.2.1. Heat transfer coefficients and temporal and spatial temperature distributions

Since most of the results were present and analysed in previous works[17,18] only relevant numerical data for further discussion are reported in Table 1. As it was expected for a convection mechanism, the surface state influenced the heat transfer giving different h values for C and F surfaces. The higher value of the coefficient for C was attributed to the increasing turbulence level caused by its inhomogeneous topography as the microstuctural features and roughness parameters revealed.[17]

In regard to the goodness of the temperature profile fitting, both points (the centre and the peripheral one) were correctly simulated with models B and C using the estimated set of fitting parameters. However, just one point was fitted using model A.[18]

3.2.2. Temporal and spatial stress distributions

3.2.2.1. Model A. According to the geometry of the thermal shock test and the attenuation model of the heat transfer coefficient, the stresses should be equibiaxial, in tension and with maximum values in the impinging zone. Fig. 1 shows the temporal evolution of the stress at the centre of the upper surface of the disk, for $T_i = 920$°C. It is confirmed that the radial and tangential stresses are equal and the component along the thickness is null. The monotonic growth of the tensile stress during the impinging time (20 s) is present in all the analysed cases.

Table 1
Temperature distributions results[b]

	T_i[a]	Model A			Model B				Model C			
		$h_0^{(1)}$[a,c]	r_{MIN}[a,c]	Fitting[d]	$h_0^{(2)}$	$h_0^{(2)'}$	r_{MIN}	Fitting	$h_0^{(2)}$	$h_0^{(2)'}$	r_{MIN}	Fitting
C	770	340	0	1	220	670	0, 5.72	2	280	850	0, 5.72	2
	850	320	0	1	205	690	0, 5.72	2	260	850	0, 5.72	2
	940	300	0	1	200	700	0, 5.72	2	250	850	0, 5.72	2
F	870	210	0	1	130	500	0, 5.72	2	160	650	0, 5.72	2
	920	230	0	1	150	500	0, 5.72	2	180	650	0, 5.72	2
	980	250	0	1	170	500	0, 5.72	2	200	650	0, 5.72	2

[a] Units: T_i in °C, h_0^i in W/m^2°C, r_{MIN} in mm.
[b] r_C for model B and C is equal to 4.74 mm for all T_i.
[c] r_{MIN} is the distance from the centre where a minimum in temperature occurs on the upper surface of the specimen.
[d] "fitting" represent the goodness of the adjustment achieved with fitting parameters reported in the table: 1: only one point can be correctly fitted (the central one). 2: both point, the centre and the peripheral one, are correctly adjusted.

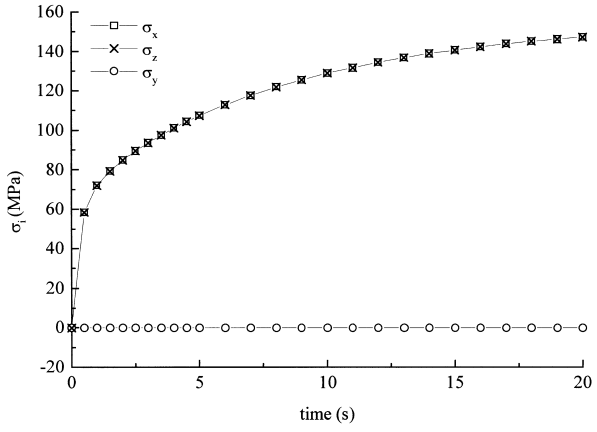

Fig. 1. Temporal evolution of the stress at the center of the upper surface for $T_i = 920$°C (model A).

In Table 2 are detailed the values of the tension in the central point of the upper surface ($\sigma_x = \sigma_z$) at 10 s (in the range of the experimental fracture time). These values are lower for F finish than for C one, in agreement with the lower coefficient h for the former (Table 1).

The spatial distribution of the stress at 10 s for T_i = 920°C are shown in contour plot for σ_x (Fig. 2a) and σ_z (Fig. 2b) and the radial variation for the central axis is drawn in Fig. 3. It is verified that the tensile stress is maximum at the centre of the tested surface of the disk. The equibiaxiality region extends over a circular area of 2 mm in radius, approximately. Outside this zone, the tangential component of the stress decreases rapidly towards the disk periphery and becomes compressive around a distance of $\approx 3.9 r_0$. Moreover, the radial component along the radius is always tensile. Along the thickness, the stresses are completely in tension up to a distance of $\approx 3.6\ r_0$ to the centre and σ_x is equal to σ_z at the central axis.

3.2.2.2. Model B. Keeping in mind the augmentation of h in the stagnation region, the position of the maximum stress cannot be predicted straightforwardly. Fig. 4 corresponds to the contour plot of the radial and tangential components of the stress at 10 s from 920°C. Conversely to model A, the stress profiles of σ_x and σ_z show local maxima. This behaviour reflects the augmentation of h in r_C that model B considers. The position of the maximum tensile stress is at the centre (where $\sigma_x = \sigma_z$) or at $r = r_M = 5.72$ mm (that occurs in σ_z) coinciding with temperature minima. At the beginning, the maximum value is always at the centre but later, σ_z grows even more

Table 2
Stress values at the upper surface of the specimen

	T_i[a]	Model A			Model B			Model C		
		σ[a]	r[a,b]	t[a]	σ	r	t	σ	r	t
C	770	130	0	10	65	0	10	77	0	4.7
	850	150	0	10	78_z[c]	5.72	10	87.5_z	5.72	2.8
	940	164	0	10	85_z	5.72	10	109_z	5.72	2.9
F	870	107	0	10	55_z	5.72	10	77_z	5.72	3.6
	920	128	0	10	60_z	5.72	10	81.5_z	5.72	3.0
	980	154	0	10	77	0	10	89_z	5.72	3.4

[a] Units: T_i in °C, σ in MPa, r in mm, t (time) in s.
[b] r is the distance from the centre on the upper surface of the specimen.
[c] when the value of the stress corresponds to the tangential component it is indicated as subscript.

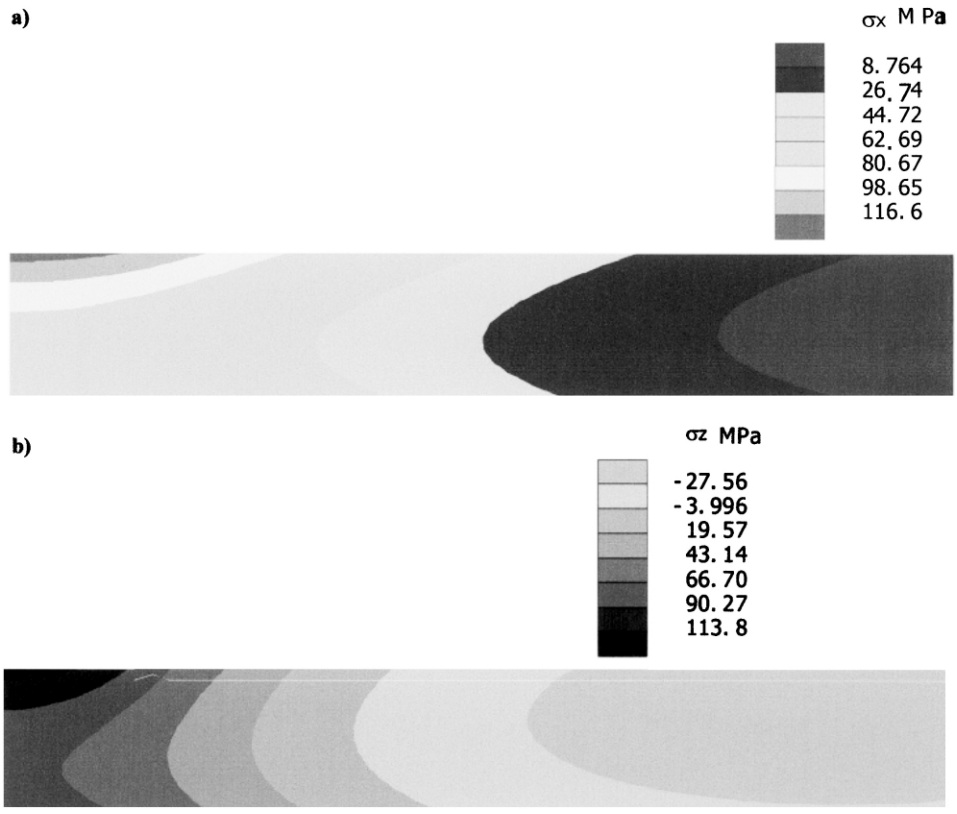

Fig. 2. Contour plot of the stress from 920°C at 10 s (model A); (a) σ_x, (b) σ_z.

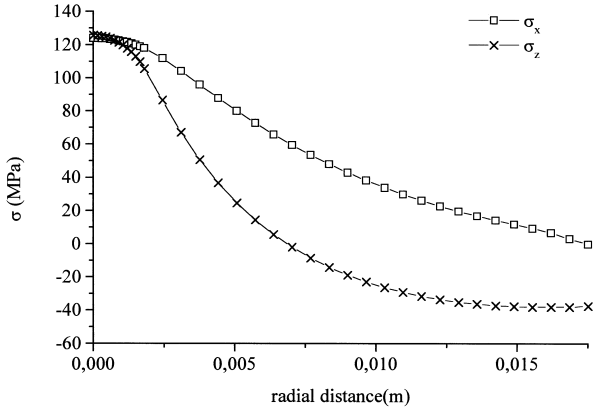

Fig. 3. Radial variation of the stress for the central axis from 920°C at 10 s (model A).

in some cases (depending on the relative magnitude of $h_0^{(2)}$ to h at r_C). Nevertheless, the radial component of the stress always exhibited a local maximum close to r_M. In Fig. 5a and b can be observed the temporal evolution of the tension at the centre and at r_M for 940°C (C) and 980°C (F), respectively, as examples of the situations that occur. In Table 2 are reported the maximum tensile stress at 10 s (fracture time) for both surface finished, C and F, and all the initial temperatures studied.

The equibiaxiality extends over a circular region with a radius of 2 mm, similar to that of model A. The tangential stress component become compressive beyond the maximum in r_M, at a distance $\approx 9r_0$ of the centre. The stress distributions along the thickness are similar to those obtained with model A being the stresses completely in tension up to a distance of $\approx 5.3r_0$ to the centre.

3.2.2.3. Model C. In most of aspects, the stresses evolution calculated with this model is analogous to that of model B even though the values of the stresses change as a consequence of the differences in boundary conditions. However, the model differs in an important point, as can be observed in Figs. 6a and b that show the temporal variation of the tensile stress at the centre and at r_M for $T_i = 940$°C (C) and 980°C (F), respectively. Conversely to model B that shows a continuous increase of the stresses with time, the profile calculated with model C present maximum values in the range 2.5–5 s. In Table 2 are reported the maximum value of σ_x and σ_z, together with the position and time, for C and F specimens and all the T_i analysed.

3.3. Discussion

The thermal stress distributions allow to give an explanation of empirical facts like the difference in ΔT_C magnitudes between C and F disks and the characteristics of crack patterns.

Based on the parity of the mechanical and thermal shock behaviour, the biaxial flexure strength and the

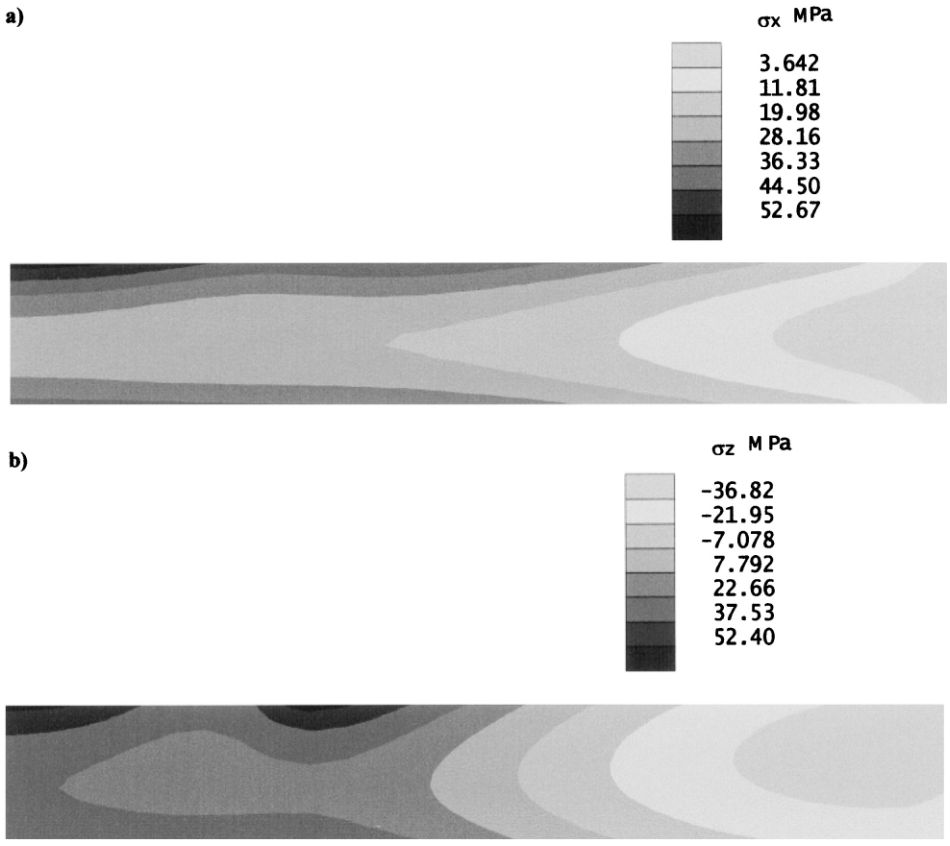

Fig. 4. Contour plot of the stress from 920°C at 10 s (model B); (a) σ_x, (b) σ_z.

maximum tensile stress at fracture time (10 s), considered as the critical thermal stress for fracture, should be comparable. However, the last values are lower than σ_F for three models (Table 2) increasing the difference in the order: A < C < B and F < C. The analysis of the area subjected to maximum tensile stress, that is related to the probability to find a critical flaw, gives a reason to this disagreement. This area can be considered as the equibiaxiality zone which is five times greater in thermal shock test (2 mm) than in biaxial flexure one (≈0.89 mm = thickness/3[24]) and, as a consequence, the probability to failure is higher for thermal shock. The greater the probability of failure, the lower the critical stress for failure. Moreover, B and C models calculations predict an additional region around r_M subjected to high tension accounting for the higher difference exhibited for these models. In regard to the finish, the calculated values are closer to σ_F for F than for C machining. This result may be attributed to an annealing effect that may relieve the residual compressive stresses in thermal shock tests because of the methodology used here in which the specimen is subjected to cumulative exposures at high temperatures during a long period each time (90 min). The presence of compressive residual stresses would modify the mechanical response of C as much as F disks[13,14,25,26] but since they are higher for the former the effect may be more pronounced on them. Finally, the higher ΔT_C values for F disks in spite of their lower mechanical strength is partially attributed to the lower tensile stresses calculated for them using any one of the models (Table 2).

The stress distributions calculated using any one of the models explain the features of the crack patterns observed. Radial and circular fisures are justified by the presence of tangential and radial tension, respectively, both high and similar in value. Moreover, the occurrence of maximum stresses beyond the impinging zone predicted by models B and C accounts for the presence of circular cracks outside this area as was observed in some specimens.

The existence of cracks that always propagate across the thickness is in accordance with the numerical calculations predicting that stresses are only in tension in the central volume of the specimen. However, these cracks often do not reach the disk periphery which is attributed to the tangential stress component becoming compressive at certain distance of the centre that depends on the model. The existence of a great volume in tension along the thickness is also considered as responsible of the high energy fracture occurring in thermal shock conditions that is evident from the fracture features like high fragmentation and tortuosity of crack path.[14]

Conversely to models A and B, model C predicts temporal maxima in stress evolutions. The times

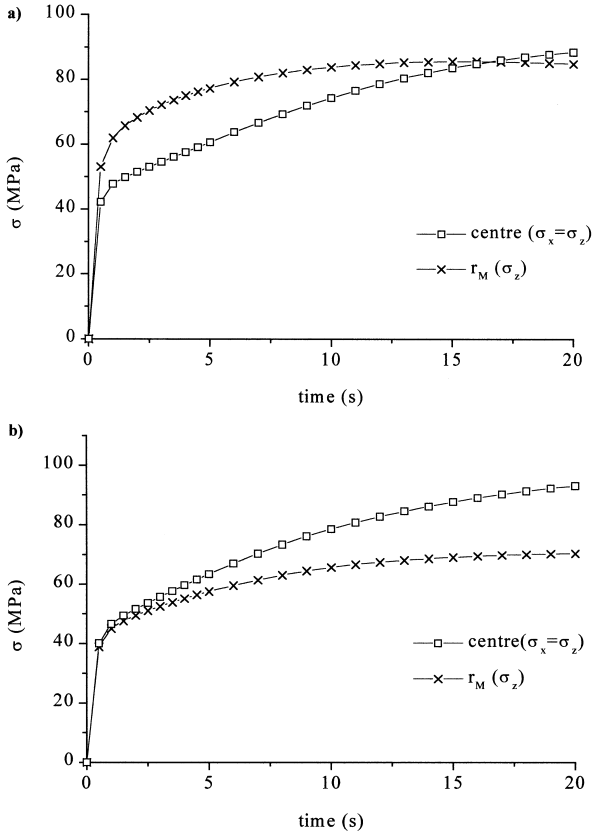

Fig. 5. Temporal evolution of stresses of the upper surface at the centre and at r_M (model B); (a) 940°C, (b) 980°C.

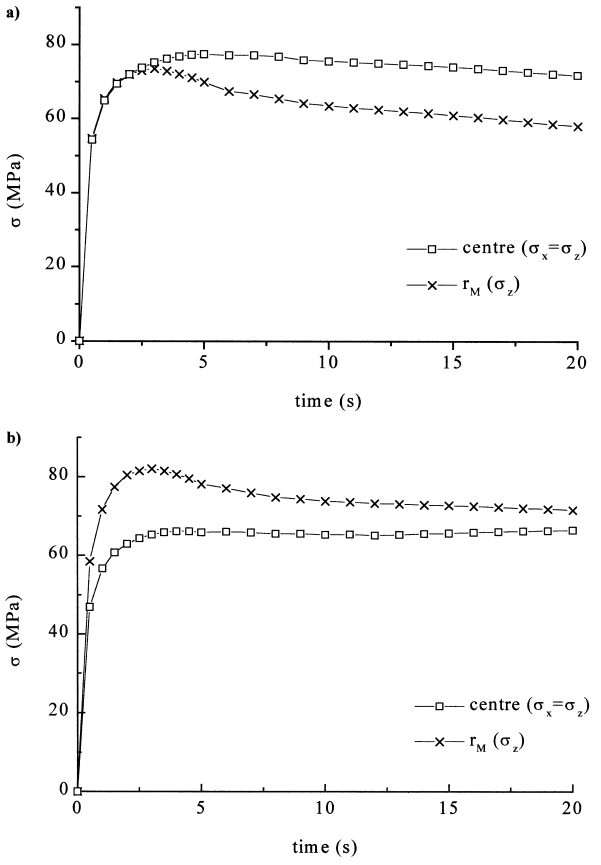

Fig. 6. Temporal variation of stresses of the upper surface at the centre and at r_M (model C); (a) 940°C, (b) 980°C.

corresponding to these maxima values are in the range of the experimental time of fracture.

3.4. Comparative analysis of the models

The numerical simulation models proposed for temperature distribution calculations during the thermal shock tests, present subsequently less and less simplifications. The increment in complexity resides in that the modelization is more close to the actual experimental conditions of the test, specifically, in regard to the heat transfer. The radial variation of the heat transfer coefficient is more realistic for models B and C with respect to model A. In addition, the consideration of heat transfer by conduction between the specimen and the refractory material in model C increases the accuracy of the boundary conditions with respect to models A and B.

The improvement in the simulation of the boundary conditions is already reflected by the fitting of the experimental registers of temperature discussed previously[18] that is better using models B and C than model A. Even though any one of the models gives reason for main empirical facts as discussed above, models B and C show a better performance than A to explain the position of cracks. In turn, model C allows to predict fracture times according with the experimental values which can not be done with the others models.

In short, the most realistic modelization of boundary conditions yield the best results to explain and support the experimental observations in the thermal shock behaviour of alumina disks. However, it is worthy to note that a simple model such as A can also be useful even though its predictions are less accurate.

Acknowledgements

The authors gratefully acknowledge CITEFA for carrying out the coarse machining of the samples and thank Norma Míngolo and María Ortíz (CNEA) for the residual stress measurements.

References

1. Faber, K. T., Huang, M. D. and Evans, A. G., Quantitative studies of thermal shock in ceramics based on a novel technique. *J. Am. Ceram. Soc.*, 1981, **64**, 296–301.
2. Niihara, K., Singh, J. P. and Hasselman, D. P. H., Observations on the characteristics of a fluidized bed for thermal shock testing of brittle ceramics. *J. Mater. Sci.*, 1982, **17**, 2553–2559.

3. Marshall, D. B., Drory, M. D., Loh, R. L. and Evans, A. G., The thermal fracture of alumina. In *Fracture in Ceramics Materials*, ed. A. G. Evans. Noyes Publications, New Jersey, 1984, pp. 336–363.
4. Johnson-Walls, D., Drory, M. D. and Evans, A. G., Evaluation of reliability of brittle components by thermal stress testing. *J. Am. Ceram. Soc*., 1985, **68**, 363–367.
5. Brockenbrough, J. R., Edgar Forsythe, L. and Rolf, R. L., Reliability of brittle materials in thermal shock. *J. Am. Ceram. Soc*., 1986, **69**, 634–637.
6. Wei, G. C. and Walsh, J., Hot-gas-jet method and apparatus for thermal-shock testing. *J. Am. Ceram. Soc*., 1989, **72**, 1286–1289.
7. Schneider, G. A. and Petzow, G., Thermal shock testing of ceramics-A new testing method. *J. Am. Ceram. Soc*., 1991, **74**, 98–102.
8. Scheneider, G. A., Thermal shock criteria for ceramics. *Ceram. Int*., 1991, **17**, 325–333.
9. Rogers, W. P. and Emery, A. F., Contact thermal shock of ceramics. *J. Mater. Sci*., 1992, **27**, 146–152.
10. Awaji, H., Oguwa, M. and Sato, S., Testing method for thermal shock fracture of ceramics. In *Third Euro-Ceramics*, vol 3, ed. P. Durán and J. F. Fernández. Faenza Editrice Iberica, Spain, 1993, pp. 883–888.
11. Olagnon, C., Fantozzi, G., Sudreau, F. and Peigne, P., Thermal shock and fatigue of mullite and alumina: refined analyses. In *Thermal Shock and Thermal Fatigue Behaviour of Advanced Ceramics*, ed. G. A. Schneider and G. Petzow. Kluwer Academic Publishers, Netherlands, 1993, pp. 371–381.
12. Urretavizcaya, G., Materiales compuestos Al_2O_3/SiC_w: síntesis, procesamiento, y caracterización. PhD thesis, Universidad Nacional de Mar del Plata, Mar del Plata, 1995.
13. Tomba M., A. G. and Cavalieri, A. L., Surface finish and mechanical strength of dense alumina. *Mater. Res. Bull*., 2000, **35**, 1077–1085.
14. Tomba M., A. G., Choque térmico de alúmina densa. PhD thesis, Universidad Nacional de Mar del Plata, Mar del Plata, 1998.
15. Poulson, B., Electrochemical measurements in flowing solutions. *Corros. Sci*., 1983, **23**, 391–430.
16. Cooper, D., Jackson, D. C., Launder, B. E. and Liao, G. X., Impinging jet studies for turbulence model assessment-I. Flow-field experiments. *Int. J. Heat Mass Transfer*, 1993, **36**, 2675–2684.
17. Tomba M., A. G. and Cavalieri, A. L., Ceramic surface finish: its influence on the heat transfer in thermal shock tests. *Mater. Lett*., 2000, **42**, 240–245.
18. Tomba M., A. G. and Cavalieri, A. L., Evaluation of the heat transfer coefficient in thermal shock of alumina disks. *Mater. Sci. Eng. A*, 2000, **276**, 76–82.
19. Gitzen, W. H., *Alumina as Ceramic Material*. The American Ceramic Society, Columbus, OH, 1970.
20. Fisher, R. E., *New Developments in Monolithic Refractories*. Advances in Ceramics, Vol. 13. The American Ceramic Society, Columbus, OH, 1985.
21. Fisher, R. E., *Advances in Refractories Technology*. Ceramic Transactions Vol. 4, The American Ceramic Society, Westerville, OH, 1988.
22. Chin, D.-T. and Tsang, C.-H., Mass transfer to an impinging jet electrode. *J. Electrochem. Soc: Electrochemic Science and Technology*, 1978, **9**, 1461–1470.
23. Tomba M., A. G. and Cavalieri, A. L., Alumina disks with different surface finish: thermal shock behaviour. *J. Eur. Ceram. Soc*., 2000, **20**, 889–893.
24. Shetty, D. K., Rosenfield, A. R., McGuire, P., Bansal, G. K. and Duckworth, W. H., Biaxial flexure tests for ceramics. *Ceram. Bull*., 1980, **59**, 1193–1197.
25. Tomlinson, W. J. and Newton, R. C., Effect of grinding, lapping and various surface treatments on the strength of silicon nitride. *Ceram. Int*., 1990, **16**, 253–257.
26. Alfaro, E., Guiheen, J., Varner, J. R., Insights provided by fractography in strength testing of machined Si_3N_4 and indented Al_2O_3. In *Fractography of Glasses and Ceramics, Ceramic Transactions*, Vol. 17, ed. V. D. Fréchette and J. R. Varner. American Ceramic Society, Westerville, OH, 1990, pp. 485–508.